



Observational Constraints on Cosmic-Ray Escape from Ultrahigh-energy Accelerators

Quentin Luce¹ , Sullivan Marafico² , Jonathan Biteau² , Antonio Condorelli² , and Olivier Deligny² ¹Karlsruhe Institute of Technology, Institute for Experimental Particle Physics (ETP), Karlsruhe, Germany; quentin.luce@kit.edu
²Laboratoire de Physique des 2 Infinis Irène Joliot-Curie, CNRS/IN2P3, Université Paris-Saclay, Orsay, France; sullivan.marafico@ijclab.in2p3.fr

Received 2022 June 2; revised 2022 July 8; accepted 2022 July 15; published 2022 August 31

Abstract

Interactions of ultra-high energy cosmic rays (UHECRs) accelerated in specific astrophysical environments have been shown to shape the energy production rate of nuclei differently from that of the secondary neutrons escaping from the confinement zone. Here, we aim at testing a generic scenario of in-source interactions through phenomenological modeling of the flux and composition of UHECRs. We fit a model in which nucleons and nuclei follow different particle energy distributions to the all-particle energy spectrum and proton spectrum below the ankle energy and distributions of maximum shower depths above this energy, as inferred at the Pierre Auger Observatory. We obtain that the data can be reproduced using a spatial distribution of sources that follows the density of extragalactic matter on both local and large scales, providing hence a realistic set of constraints for the emission mechanisms in cosmic accelerators, for their energetics, and for the abundances of elements at escape from their environments. While the quasi monoenergetic increase of the cosmic-ray mass number observed on Earth from $\simeq 2$ EeV up to the highest energies calls for nuclei accelerated with a hard spectral index, the inferred flux of protons down to $\simeq 0.6$ EeV is shown to require for this population a spectral index significantly softer than that generally obtained up to now. We demonstrate that modeling UHECR data across the ankle substantiates the conjecture of in-source interactions in a robust statistical framework, although pushing the mechanism to the extreme.

Unified Astronomy Thesaurus concepts: Particle astrophysics (96); Ultrahigh-energy cosmic radiation (1733); Cosmic-ray sources (328); Astronomy data modeling (1859); Secondary cosmic rays (1438); Spectral index (1553)

1. Introduction

The sources of ultra-high energy cosmic rays (UHECRs) remain unknown. Their identification relies primarily on capturing in the UHECR arrival directions a pattern suggestive in an evident way of a class of astrophysical objects. Such a capture is still eluding our grasp, but some recent observations have allowed broad statements to be drawn. An anisotropy at large scales has been revealed above $\simeq 8$ EeV (Aab et al. 2017a), the contrast and the direction of which are consistent with expectations drawn from sources distributed in a similar manner to extragalactic matter (Aab et al. 2017a, 2018a). At higher energies ($\gtrsim 40$ EeV), a correlation between UHECR arrival directions and the flux patterns of massive, star-forming or active galaxies within 200 Mpc provide evidence for anisotropy (Aab et al. 2018b; Biteau & Pierre Auger Collaboration 2021). Overall, these observations suggest that UHECRs are predominantly of extragalactic origin at least above the so-called ankle energy at $\simeq 5$ EeV.

The energy spectrum and chemical composition of UHECRs observed on Earth result from the emission processes at play, which encompass acceleration mechanisms, losses and escape from the source environments, as well as propagation effects. Different from, and complementary to, anisotropies, these two observables provide constraints that help infer the properties of the acceleration processes, the energetics of the sources, and the abundances of elements in the source environments. Following this principle, several studies have laid the foundations for a generic scenario that broadly reproduces the

observations (Allard et al. 2008; Aloisio et al. 2014; Taylor et al. 2015; Aab et al. 2017b; Zhang et al. 2018; Guido & Pierre Auger Collaboration 2021). The intensity of the individual nuclear components at the sources, generally considered as stationary and uniformly distributed in a comoving volume, is assumed to drop off at the same magnetic rigidity so as to explain the gradual increase with energy of the mass number A observed on Earth (Abraham et al. 2010; Aab et al. 2014a; Watson 2022). This is consistent with the basic expectation that electromagnetic processes accelerate particles up to a maximum energy proportional to their electric charge Z . Most notably, the abundance of nuclear elements is found to be dominated by intermediate-mass ones, ranging from He to Si, accelerated to $E_{\max}^Z \simeq 5Z$ EeV and escaping from their source environments with a very hard spectral index γ (that characterizes the emission spectrum at the sources as $E^{-\gamma}$), which, depending on the systematic uncertainties affecting some of the necessary modeling, ranges between $\gamma \simeq -1$ and $\gamma \simeq 1$ (Aab et al. 2017b).

Reaching ultra-high energies can be most easily achieved by first-order Fermi shock acceleration, where particles are energized by bouncing back and forth across moving magnetic fields (see, e.g., Sironi et al. 2015 for a review). While the typical spectral index for this mechanism ($\gamma \gtrsim 2$) appears to deviate significantly from the hard values favored from the data, the interplay between the escape from the sources and the acceleration mechanisms must be taken into account to apprehend correctly the emission spectrum (e.g., Fujita et al. 2009), in particular when escape is influenced by in-source interactions (Globus et al. 2015; Unger et al. 2015; Biehl et al. 2018; Fang & Murase 2018; Zhang et al. 2018; Supanitsky et al. 2018; Boncioli et al. 2019; Muzio et al. 2022). The cosmic-ray luminosity of the source candidates is governed,



Original content from this work may be used under the terms of the [Creative Commons Attribution 4.0 licence](https://creativecommons.org/licenses/by/4.0/). Any further distribution of this work must maintain attribution to the author(s) and the title of the work, journal citation and DOI.

among other things, by the levels of radiation and magnetic-field densities. While gaining energy, UHECRs can interact with this radiation or escape from the magnetized zone. Thus, the energy spectrum of the ejected particles as well as the amount of ejected nuclei may differ strongly from those injected into the electromagnetic field. This has two important consequences: (a) the ejected spectrum of the charged nuclei can be much harder than that injected, due to the escape mechanism and in particular the behavior of the nuclei-photon cross section at high energies; and (b) the interactions can produce a copious flux of secondary neutrons of energy $E_n = E/A$. These neutrons can escape freely from the magnetic confinement zones, with an ejection spectrum much softer than that of nuclei, to decay into protons on their way to the Earth after an average travel distance of $9.1 \text{ kpc} \times (E_n/1 \text{ EeV})$.

In this paper, we derive constraints on the characteristics of the sources by searching for a robust statistical agreement between data and predictions based on realistic astrophysical ingredients and on a phenomenological model incorporating in-source interactions in an effective way. The agreement is sought for both spectral and mass composition data, while only a qualitative overview of the latter has been performed so far in studies incorporating in-source interactions. To do this, we consider the data obtained at the Pierre Auger Observatory beyond 0.63 EeV ($10^{17.8} \text{ eV}$). However, and different from the approaches adopted elsewhere, only the proton spectrum is used in the energy range between 0.63 and 5 EeV . This approach allows us to reconstruct the extragalactic component without resorting to any introduction of *ad hoc* nuclear components to model what is generally assumed to be the upper end of the galactic component so as to reproduce the average mass composition as a function of energy. Such modeling, suffering from both observational systematics and theoretical unknowns, blurs reconstruction of the extragalactic proton component with biases inherent to the choices made. In the same spirit, we do not attempt to sew together the Auger observations with those made in an energy range half-a-decade lower with the KASCADE-Grande detector mixing indistinctly protons and helium (Apel et al. 2012), always with the aim of reconstructing the proton component as precisely as possible.

With this approach, we show that a scenario incorporating in-source interactions can reproduce the data and that accounting for the local overdensity of galaxies within tens of Mpc further improves the goodness of fit with respect to the generally assumed uniform distribution of sources in a comoving volume. Quantitatively, we show that the analysis of data from the Pierre Auger Observatory significantly favors an effective spectral index of protons ejected from the sources that is softer than generally obtained or assumed, somehow pushing the in-source interaction mechanism to the extreme. At the same time, we point out that this spectral index approaches more canonical values provided that all protons are secondaries of the interactions, i.e., that the environment of the sources is devoid of protons to be accelerated.

This paper is organized as follows. In Section 2, we motivate the model used to probe those effects and set up a benchmark scenario among the ingredients needed to propagate the particles from their sources to the Earth. The data and fitting method are presented in Section 3. Results obtained with the benchmark scenario are given in Section 4, where we explore as well the impact of changing the ingredients that are affected

by systematic uncertainties. Finally, the significance of the results is discussed in Section 5.

2. Generic Model of UHECR Production with In-source Interactions

The benchmark astrophysical model used here is inspired by that of Aab et al. (2017b) for its main features. The non-thermal processes responsible for accelerating the different particles are modeled through power-law spectra as long as the energies are sufficiently below the Z -dependent maximal acceleration energy $E_{\text{max}}^Z = ZE_{\text{max}}$, while, in the absence of any firmly-established prescription from theory, exponential suppression is used for modeling the upper end of the acceleration process. The sources are assumed to accelerate different amounts of nuclei represented by five stable ones: hydrogen (^1H), helium (^4He), nitrogen (^{14}N), silicon (^{28}Si), and iron (^{56}Fe). The unavoidable fluctuations of the characteristics of each individual source are neglected, considering all sources as identical. This is a simplification that renders the number of free parameters manageable in a fitting procedure. The fitted parameters should be interpreted as effective ones, describing the average spectrum of the source population.

Modeling the ejection spectra in terms of power laws suppressed at the highest energies is an approximation aimed at keeping, once again, the number of free parameters to a minimum. However, detailed studies of the nuclear cascade developing in sources from photodissociation with different levels of radiation densities, such as that presented by Biehl et al. (2018), show that such a simplification holds in the energy range of interest for this study. This is also true for the softer flux of secondary neutrons produced during the development of the cascade, which dominates over that of the ejected protons. We generically model the ejection rate per comoving volume unit and per energy unit of nucleons as

$$q_p(E) = q_{0p} \left(\frac{E}{E_0} \right)^{-\gamma_p} f_{\text{supp}}(E, Z_p), \quad (1)$$

with $Z_p = 1$, that is a single reference ejection rate q_{0p} , spectral index γ_p and suppression function $f_{\text{supp}}(E, Z_p)$ for both escaping protons and protons from neutron decay. Here, E_0 is arbitrarily set to 1 EeV . The ejection rate of nuclei with mass number A_i is also generically modeled as

$$q_{A_i}(E) = q_{0A_i} \left(\frac{E}{E_0} \right)^{-\gamma_{A_i}} f_{\text{supp}}(E, Z_{A_i}), \quad (2)$$

that is a single spectral index γ_{A_i} and four independent reference ejection rates q_{0A_i} for helium, nitrogen, silicon, and iron. As in the reference scenario of Aab et al. (2017b), the suppression function adopted both for nucleons and nuclei is taken as

$$f_{\text{supp}}(E, Z) = \begin{cases} 1 & \text{if } E \leq E_{\text{max}}^Z, \\ \exp(1 - E/E_{\text{max}}^Z) & \text{otherwise.} \end{cases} \quad (3)$$

The maximum acceleration energy is assumed to be proportional to the electric charge of each element, $E_{\text{max}}^Z = ZE_{\text{max}}$, with a single free parameter E_{max} shared by the five species.

In this approach, the ejection rate for protons accounts for both the accelerated ones up to E_{max} and those produced by the escaping neutrons, inheriting hence an energy of the order of E/A from the nuclei of energy E . The maximum energy that

this population of secondary protons can reach is then $E_{\max}^Z/A \simeq E_{\max}/2$, which is not reflected in the rigidity-acceleration scheme modeled by Equation (3). The extreme case in which all ejected protons would be photodissociation by-products can be tested by replacing E_{\max} by $E_{\max}/2$ in $q_p(E)$. We will explore this extreme case in Section 4. Further characterization of the balance between the population of accelerated protons from the initial abundance in the source environment and that of secondaries from nuclear cascades calls for modeling of specific sources and environments, which is beyond the scope of this paper.

The differential energy production rate per comoving volume unit of the sources, which is directly related to their differential luminosity, is then $\ell_j(E, z) = E^2 q_j(E) S(z)$ for each species j , where $S(z)$ describes the redshift evolution of the UHECR luminosity density. The quantity $\ell_j(E, z)$ is hereafter called the differential energy production rate for convenience. On the other hand, the bolometric energy production rate per comoving volume unit at redshift z is obtained as $\mathcal{L}_j(E, z) = S(z) \int_E^\infty dE' E' q_j(E')$. We hereby report its average value in a volume spanning $z_{\min} - z_{\max}$ as $\bar{\mathcal{L}}_j(E) = \int_{z_{\min}}^{z_{\max}} dz \left| \frac{dt}{dz} \right| \mathcal{L}_j(E, z) / \int_{z_{\min}}^{z_{\max}} dz \left| \frac{dt}{dz} \right|$, where $t(z)$ is the lookback time.

The evolution of the UHECR luminosity density is taken as being traced by the density of baryonic matter over cosmic time. The latter is assumed to follow the density of stellar mass, which is fairly approximated by a constant out to redshift $z = 1$ (e.g., Madau & Dickinson 2014). As in the benchmark scenario of Aab et al. (2017b), such a constant evolution is assumed to hold to first approximation out to $z_{\max} = 2.5$. The local universe presents however an overdensity because, like most galaxies, the Milky Way belongs to a group of galaxies, itself embedded in the Local Sheet (McCall 2014). We adopt here the overdensity correction factor inferred by Condon et al. (2019) expressed as a function of the distance r and effective up to 30 Mpc

$$\frac{\delta\rho(r)}{\bar{\rho}} = 1 + \left(\frac{r}{r_0} \right)^{-\alpha}, \quad (4)$$

with $r_0 = 5.4$ Mpc and $\alpha = 1.66$. The evolution of the UHECR luminosity density is then described as $S(z) = \delta\rho/\bar{\rho}$, with $z_{\max} = 2.5$ and $z_{\min} = 2 \times 10^{-4}$. The minimum redshift, which corresponds to the limit of the Local Group of galaxies ($r \simeq 1$ Mpc), prevents any divergence in Equation (4) and effectively removes very closeby galaxies that would otherwise dominate the UHECR sky, at odds with observations.

Extragalactic magnetic fields are poorly known, except for upper limits at the nG level from rotation measures (Pshirkov et al. 2016; O’Sullivan et al. 2020) or down to tens of pG for magnetic fields of primordial origin that would affect CMB anisotropies (Jedamzik & Saveliev 2019). Lower limits at the fG level have also been derived from the non-observation in the GeV range of gamma-ray cascades from TeV blazars (Neronov & Vovk 2010; Tavecchio et al. 2010; Ackermann et al. 2018). These non-observations have been interpreted as the deflection of the cascade flux into a broadened beam weakening the point-like image, noting though that the lower limits could be alleviated if plasma instabilities dominated the cooling rate of particles in the cascade (see Alves Batista & Saveliev 2021; Biteau & Meyer 2022, for recent reviews). While field values

saturation the limits from rotation measures might impact the results by reducing the UHECR horizon (Mollerach & Roulet 2013; Wittkowski 2018), we assume here that magnetic fields in cosmic voids are at the level of 0.1 nG or less, as suggested by cosmological magnetohydrodynamical simulations (Vazza et al. 2017). In this case, they do not have sizeable effects on the propagation of the particles, which can therefore be considered one dimensional.

The all-particle energy spectrum $J(E)$ observed at present time thus results from the integration of the contribution of all sources over lookback time, the role of which is played by redshift as

$$J(E) = \frac{c}{4\pi} \sum_{A, A'} \iint dz dE' \left| \frac{dt}{dz} \right| S(z) q_{A'}(E') \frac{d\eta_{AA'}(E, E', z)}{dE} \quad (5)$$

Here, the relationship between cosmic time and redshift follows from the concordance model used in cosmology, $(dt/dz)^{-1} = -H_0(1+z)\sqrt{\Omega_m(1+z)^3 + \Omega_\Lambda}$, where $H_0 = 70 \text{ km s}^{-1} \text{ Mpc}^{-1}$ is the Hubble constant at present time, $\Omega_m \simeq 0.3$ is the density of matter (baryonic and dark matter), and $\Omega_\Lambda \simeq 0.7$ is the dark-energy density. The energy losses and spallation processes are described by $\eta_{AA'}(E, E', z)$, which is the fraction of particles detected on Earth with energy E and mass number A from parent particles emitted by sources with energies $E' > E$ and mass numbers $A' > A$. In practice, for a given source with redshift z_0 emitting a nuclear species A_0 at energy E_0 , the corresponding $\eta_{A_0 A'}(E_0, E', z_0)$ function is tabulated in bins of A' and E' by propagating a large number of emitted particles ($O(10^7)$ particles) using the SimProp package (Aloisio et al. 2012, 2015, 2016). By repeating the simulations for different values of z_0 , A_0 , and E_0 , the whole $\eta_{AA'}(E, E', z)$ function is tabulated as a 5D histogram, providing hence the fractions being sought. The relevant processes accounted for in SimProp are pair production, photopion production, and photodissociation off the photon fields of interest, which are those from the cosmic microwave background (CMB) radiation, and the infrared photons from the extragalactic background light (EBL) that comprises the radiation produced in the universe since the formation of the first stars. The CMB radiation is characterized as a blackbody spectrum with a redshift-dependent temperature $T(z) = T_0(1+z)$, with $T_0 = 2.725$ K. The EBL is less precisely known, especially in the far-infrared and at high redshifts. For the benchmark scenario explored below, we use the model of Gilmore et al. (2012) that is consistent with the minimal intensity level from galaxy counts and with indirect measurements from absorption of gamma-rays at multi-TeV energies (see, e.g., Pueschel & Biteau 2021, for a recent review). Alternative EBL models are studied as sources of systematic uncertainties. Pair production is a very well-known process that results in a small fractional energy loss above a threshold of $\simeq 0.5A \epsilon_{\text{meV}} \text{ EeV}$, with ϵ_{meV} the energy of the photon targets in meV. Photopion cross sections have been measured in accelerator-based experiments and are well reproduced by various event-generator codes. The corresponding fractional energy loss is quite important above a threshold of $\simeq 30A \text{ EeV}$, causing the Greisen–Zatsepin–Kuzmin (GZK) effect. Photodissociation cross sections for

nuclei, on the other hand, are less known, especially for exclusive channels in which charged fragments are ejected. The fractional energy losses used here, which also shape the suppression of the spectrum, rely on phenomenological approaches, using the TALYS model (Koning et al. 2005; Koning & Rochman 2012) for the benchmark scenario. We also evaluate alternative models as sources of systematic uncertainties. In any event, because the binding energies are of order of a few MeV for all nuclei of interest, the center-of-mass energy depends only on the Lorentz factor of the nuclei. For heavy nuclei like iron, the photodissociation thus occurs for higher-energy photons—infrared background photons with energies about an order of magnitude higher than the typical CMB photon energy. Since these photons are less abundant than the CMB ones, the attenuation of heavy nuclei is relatively slow and is comparable to that of protons. On the other hand, the Lorentz factor is high enough for light nuclei to photodissociate by CMB background photons and their attenuation is much faster than that of protons. Finally, the adiabatic losses due to the expansion of the universe are included in the energy-loss rate of the particles as $-(1/E)(dE/dt) = -((1+z)dt/dz)^{-1}$.

With these ingredients, Equation (5) can be used to evaluate the all-particle flux from the various contributions of each individual nuclear component on the condition to assign values to the five ejection rates q_{0A} , the two indices γ_p and γ_A , and the maximum energy E_{\max} . These eight parameters are fitted to the data in the way explained in the next section.

3. Combined Fit to the Energy-spectrum and Mass-composition Data

The expected spectrum modeled by Equation (5) depends on several unknown parameters characterizing the properties of the acceleration processes, of the source environments, and of the source energetics. The observed energy spectrum and mass composition can, as discussed in Section 1, provide constraints helping in inferring these parameters.

The data we use hereafter are those obtained at the Pierre Auger Observatory, located in the province of Mendoza (Argentina) and providing the largest exposure to date of UHECRs (Aab et al. 2015). The Observatory is a hybrid system that detects the extensive air showers induced in the atmosphere subsequent to the collisions of UHECRs with nitrogen and oxygen molecules. We shall make use on the one hand of the all-particle energy spectrum inferred from these data (Abreu et al. 2021), and on the other hand of the distributions of the slant depth of maximum shower development (X_{\max}), which is a proxy, the best up to date, of the primary mass of the particles (Aab et al. 2014a; Bellido & Pierre Auger Collaboration 2018). With caution over the hadronic-interaction generators used to model the development of the showers, the X_{\max} distributions allow for inference of the energy-dependent mass composition on a statistical basis. Two hadronic-interaction generators are considered here, namely EPOS-LHC (Pierog et al. 2015) for the benchmark scenario and Sibyll2.3 c (Riehn et al. 2017) as an alternative, which are up to date and best describe the data. Hence, the various mass components $J_i(E)$ can be derived by combining the all-particle energy spectrum and the abundances of the different elements as a function of energy. The energy threshold considered here

is the nominal one of the detection mode of X_{\max} at ultra-high energies, namely $\simeq 0.63$ EeV ($10^{17.8}$ eV). Incidentally, this threshold allows us to explore the energy range of the ankle feature.

From a set of proposed parameters Θ , the best match between the observed spectrum and that expected from Equation (5) is obtained through a Gaussian likelihood fit. Under the assumption that the transition to extragalactic UHECRs is already completed above 5 EeV,³ the corresponding likelihood term, L_J , is calculated above that threshold. The model is fitted to the X_{\max} data, following Aab et al. (2017b), using a multinomial distribution that describes how likely it is to observe, in each energy bin m , k_{mx} events out of n_m with probability p_{mx} in each X_{\max} bin. The probabilities p_{mx} are obtained by using generators of hadronic interactions to model the X_{\max} distributions expressed in terms of the proposed parameters Θ . The corresponding likelihood term, $L_{X_{\max}}$, is built as the product over energy bins above 5 EeV. The last contribution to the likelihood stems from the sub-ankle proton component, L_{J_p} , obtained by weighting the all-particle spectrum below 5 EeV with the proton abundance $f_p(E)$ from the X_{\max} distributions. The statistical uncertainties in $\hat{J}_p(E)$ are dominated by those in $f_p(E)$ and are accounted for through a Gaussian likelihood fit.

The model likelihood is therefore given by $L = L_J L_{X_{\max}} L_{J_p}$. The goodness of fit is assessed with a deviance, D , defined as the negative log-likelihood ratio of a given model and the saturated model that perfectly describes the data

$$D = -2 \log \frac{L_J}{L_J^{\text{sat}}} - 2 \log \frac{L_{X_{\max}}}{L_{X_{\max}}^{\text{sat}}} - 2 \log \frac{L_{J_p}}{L_{J_p}^{\text{sat}}}. \quad (6)$$

The three different contributions are referred to as D_J , $D_{X_{\max}}$, and D_{J_p} , respectively.

4. Results

Fitting the model to the data within the framework of the benchmark scenario described in Section 2, with free spectral indices for both nucleons and nuclei ($\gamma_p \neq \gamma_A$), leads to the parameters and deviance given in Table 1 using EPOS-LHC to interpret the X_{\max} data (results obtained using Sibyll2.3 c are given in Appendix C for completeness). For reference, Table 1 also provides the results obtained under the assumption of a proton component dominated by neutron escape (proton maximum energy of $E_{\max}/2$), of no local overdensity (widely used uniform distribution), and of a shared spectral index across the five species ($\gamma_p = \gamma_A$).

Similarly to that found by Aab et al. (2017a), the value of E_{\max} , determined by the drop in the nuclear components at E_{\max}^Z , implies that the suppression of the spectrum is due to the combination of the cut-off energy at the sources for the heavier nuclei and the energy losses en route. The spectral index of the nuclei, γ_A , is in turn determined by the increase of the average mass with energy, which is almost mono-elemental, so as to reproduce the X_{\max} distributions as well as possible. The solution provided by the fit therefore consists of imposing a hard index for nuclei so that the contribution of each element mixes as little as possible: high-energy suppression imposed by the cut-off beyond E_{\max}^Z and low-energy suppression via the

³ We checked that a moderate increase in the value at which the transition to extragalactic UHECRs is assumed to be completed has no significant impact on the results.

Table 1
Best-fit Parameters and Minimum Deviance

Scenario	γ_p	γ_A	$\log_{10} E_{\max}$ (eV)	$\tilde{\mathcal{L}}_p/\mathcal{L}_0$	$\tilde{\mathcal{L}}_{\text{He}}/\mathcal{L}_0$	$\tilde{\mathcal{L}}_N/\mathcal{L}_0$	$\tilde{\mathcal{L}}_{\text{Si}}/\mathcal{L}_0$	$\tilde{\mathcal{L}}_{\text{Fe}}/\mathcal{L}_0$	D/ndf
Benchmark	3.24 ± 0.10	-0.46 ± 0.03	18.35 ± 0.01	5.51 ± 0.22	1.71 ± 0.14	2.99 ± 0.17	0.59 ± 0.14	0.02 ± 0.03	236.8/125
$E_{\max}^p = E_{\max}/2$	2.47 ± 0.19	-0.42 ± 0.02	18.37 ± 0.01	5.23 ± 0.37	1.68 ± 0.14	3.14 ± 0.47	0.50 ± 0.99	0.05 ± 0.04	235.8/125
No overdensity	3.25 ± 0.14	-0.68 ± 0.03	18.32 ± 0.01	5.41 ± 0.21	1.86 ± 0.14	2.72 ± 0.14	0.95 ± 0.25	0.09 ± 0.14	256.9/125
$\gamma_p = \gamma_A$	γ_A	-1.54 ± 0.10	18.19 ± 0.01	0.63 ± 0.07	1.44 ± 0.14	3.09 ± 0.08	0.34 ± 0.21	0.12 ± 0.02	862.7/126

Note. Column one lists the scenarios: the benchmark features different spectral indices for nucleons and nuclei, a cut-off energy for each component at $E_{\max}^Z = ZE_{\max}$, as well as an evolution of sources that is flat at large distances and follows the local overdensity of matter within 30 Mpc. Subsequent lines provide the results for scenarios differing from the benchmark as follows: a nucleon maximum energy equal to that of escaping neutrons ($E_{\max}^p = E_{\max}/2$), a strictly flat evolution (no overdensity), and a shared index across nucleons and nuclei ($\gamma_p = \gamma_A$). Columns two and three provide the spectral indices of nucleons and nuclei, respectively. Column four provides the maximum energy of nucleons. The subsequent five columns provide the bolometric energy production rate for each species above $10^{17.8}$ eV, normalized to a reference value of $\mathcal{L}_0 = 10^{44}$ erg Mpc $^{-3}$ yr $^{-1}$. The last column provides the deviance obtained with the best-fit parameters as well as the number of degrees of freedom (ndf). The uncertainties on the parameters of the E - and Z -dependence of the ejection rate (columns 2–4) are obtained through a profile likelihood. Those on the bolometric energy production rate (columns 5–9) are obtained from the inverse Hessian matrix, for the parameters in columns 2–4 fixed to their best-fit values.

hard index γ_A . However, this phenomenon does not apply to protons, which are present in an energy range where a mixture of elements is required. The best-fit value of γ_p is much softer than that of γ_A . Note that the introduction of γ_p significantly improves the fit of the data down to 0.63 EeV, with a total deviance of $D=236.8$ compared to 862.7 in the case of $\gamma_p = \gamma_A$ so that the introduction of this extra free parameter is amply justified. On the other hand, the introduction of the local overdensity to trace the source distribution also provides a substantial improvement of the deviance, although with moderate impact on the best-fit parameters.

The balance regulating the intensity of each component is reported in terms of the energy production rates $\tilde{\mathcal{L}}$ above 0.63 EeV. The solution is illustrated in Figure 1, where the contributions of each nuclear component to the observed energy flux and energy density are displayed. In Figure 2, the energy production rates required at the sources to fuel the observed energy flux are shown as a function of energy for the different primary mass groups. While the contribution of nuclei peaks at most to $\simeq 5 \times 10^{44}$ erg Mpc $^{-3}$ yr $^{-1}$ dex $^{-1}$, that of protons is increasing up to $\simeq 10^{45}$ erg Mpc $^{-3}$ yr $^{-1}$ dex $^{-1}$ when going down in energy. Extrapolations of the results below 0.63 EeV are however hazardous, as the functional shape used in Equation (1) may not hold anymore depending on the specifics of the source environments that govern the nuclear cascade. Integrated above 0.63 EeV, the total energy production rate is found to be $(10.8 \pm 0.4) \times 10^{44}$ erg Mpc $^{-3}$ yr $^{-1}$. For completeness, the X_{\max} distributions used in this work together with the best-fit models obtained within the benchmark scenario explored here are shown in Appendix A (Figure 3).

The reduced deviance is decomposed into three terms, according to Equation (6). As detailed in Appendix B, the spectral sector leads to an acceptable fit ($D_j + D_{j_p} = 37.3$ for $N_j + N_{j_p} = 24$ points). As in Aab et al. (2017a), the X_{\max} sector is more difficult to fit as evidenced by the value $D_{X_{\max}} = 199.5$ for $N_{X_{\max}} = 109$ points. The large value of the deviance on X_{\max} reflects the difficulty for hadronic-interaction generators to reproduce the data, as illustrated in Appendix A. In general, the benchmark scenario fits the data with similar performance to that obtained by considering only data beyond 5 EeV. Considering the variation of Equation (1) that consists in substituting E_{\max} for $E_{\max}/2$ yields the results reported in the fourth line of Table 2. It is interesting that the main changes concern the spectral index of the protons, which becomes

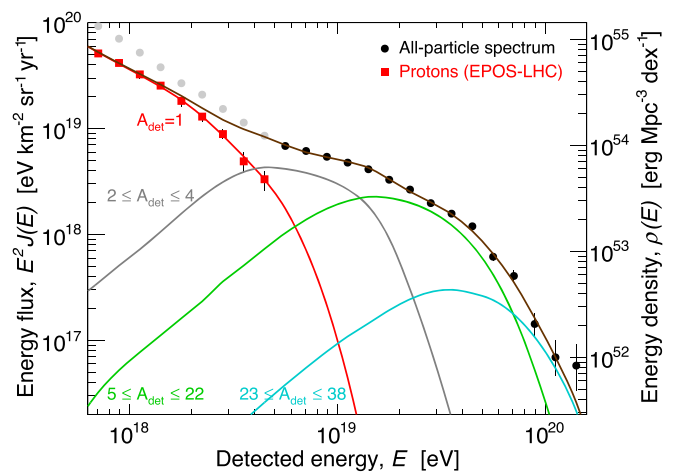


Figure 1. Energy flux at Earth as a function of energy, as modeled by the best-fit parameters for the benchmark scenario. The all-particle spectrum and proton component are shown as black circles and red squares, respectively. Lighter points are not included in the fit. The best-fit components obtained for the five detected mass groups are displayed with solid colored lines, as labeled in the figure. The energy flux of the heaviest mass group, with detected mass numbers of 39–56, is below the range of interest.

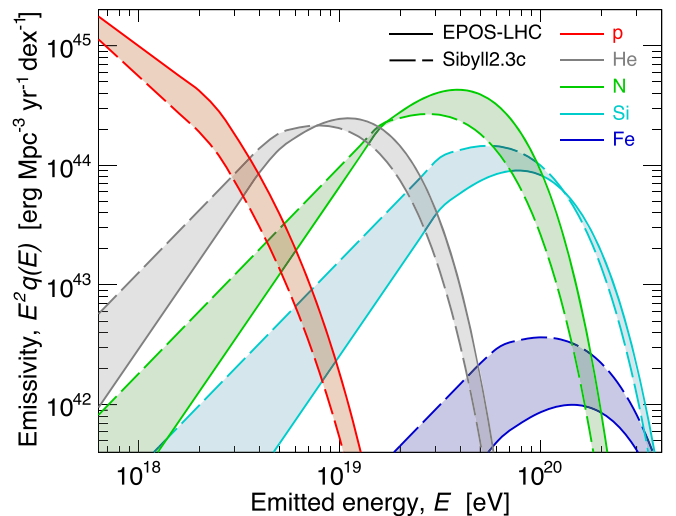


Figure 2. Mass-dependent energy production rate at the sources as a function of energy, as constrained by the best-fit parameters for the benchmark scenario. The dashed lines illustrate a variation of the hadronic interaction model, with EPOS-LHC and Sibyll2.3 c shown as solid and dashed lines, respectively.

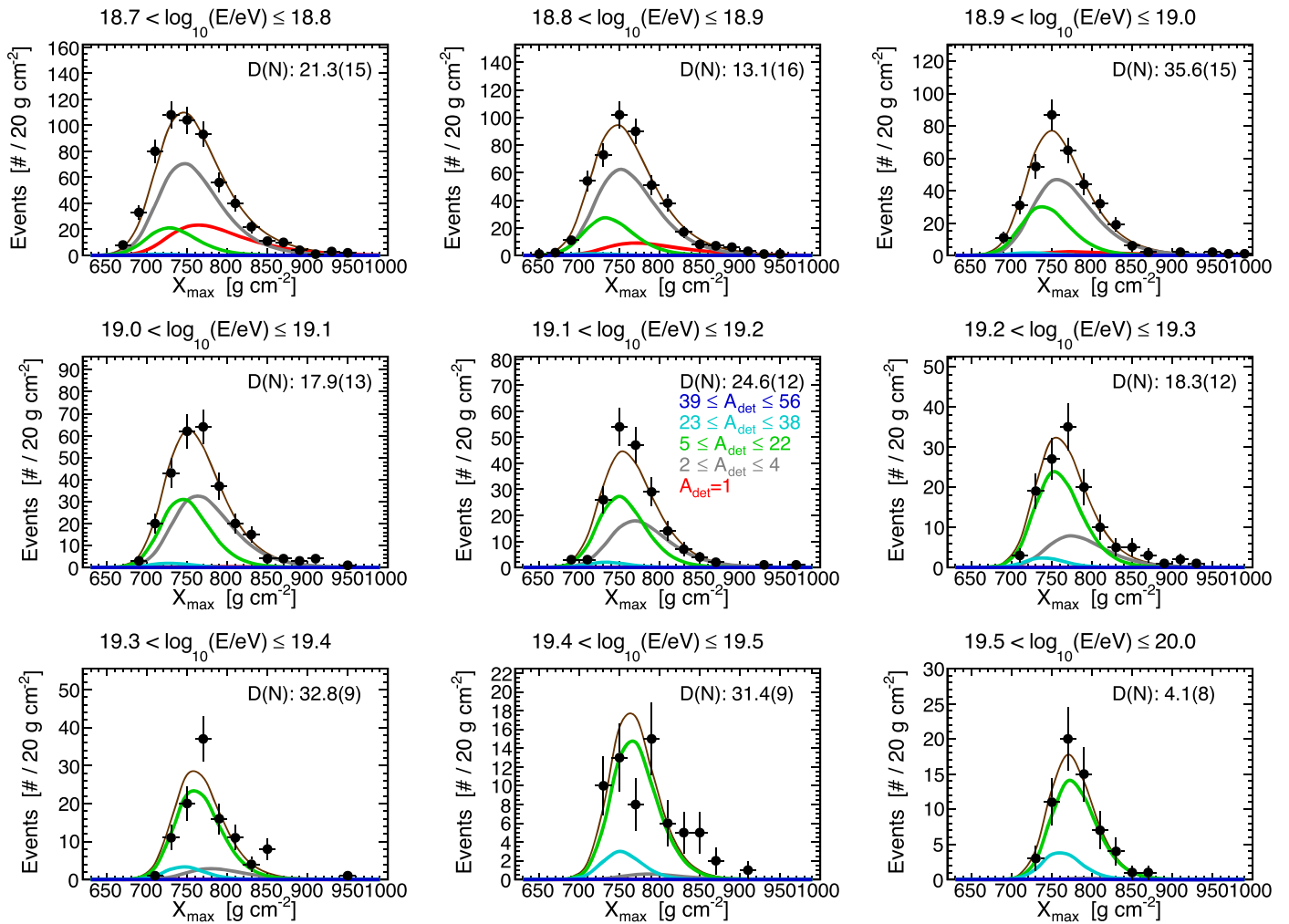


Figure 3. Distributions of the shower-depth maximum, X_{\max} , for the best-fit models. The contributions of the five detected mass groups are displayed with solid colored lines, as labeled in the figure. The sum of the five contributions is shown in brown. The deviance (D) and number of points (N) are shown in the top-right corner of each plot for each energy bin. Note that one event at $1,070 \text{ g cm}^{-2}$ is out of the displayed X_{\max} range for $18.9 < \log_{10}(E/\text{eV}) \leq 19.0$.

Table 2
Breakdown of the Deviance for the Benchmark Scenario

Scenario	$D_J (N_J)$	$D_{J_p} (N_{J_p})$	$D_{X_{\max}} (N_{X_{\max}})$	D/ndf
$\gamma_p \neq \gamma_A$	36.4 (15)	000.9 (9)	199.5 (109)	236.8/125
$\gamma_p = \gamma_A$	25.9 (15)	632.0 (9)	204.8 (109)	862.7/126

Note. Column one and five list the scenarios and deviance as in Table 1. Columns 2–4 provide a breakdown of the deviance as in Equation (6) and the number of points N associated to each term.

$\gamma_p \simeq 2.5$. The astrophysical consequences of these results will be discussed in Section 5, after the sources of systematic uncertainties have been discussed below.

The inferred mass-dependent energy production rates, tracing directly the abundances of elements escaping from the source environments, rely primarily on the X_{\max} distributions. The systematic uncertainties in X_{\max} , which are slightly energy-dependent and range from 6 to 9 g cm^{-2} (Aab et al. 2014b), are thus expected to impact the results. A reduction of the X_{\max} scale by 1σ , which results in an overall heavier composition on Earth, has as a main impact a decrease of the proton and helium contributions by, respectively, $\simeq 15\%$ and $\simeq 35\%$, with an increase of the spectral index γ_A of $+0.7$. This configuration

leads to a deviance improvement of $\simeq 16$ units. On the other hand, an increase of the X_{\max} scale by 1σ deteriorates the quality of the fit in an untenable way (more than 100 units of deviance), as the overall lighter composition implied is then in tension with the width of the X_{\max} distributions. By contrast, the inferred parameters and quality of the fits are mildly altered by the systematic uncertainties affecting the energy spectrum, which are dominated by those in the energy scale ($\Delta E/E = 14\%$). This is because a change in E_{\max}^Z can be reproduced by slightly different balances regulating the intensity of each nuclear component due to the dependence of the photodisassociation threshold with the mass number A of the nuclei.

The interpretation of the X_{\max} distributions heavily relies on the hadronic-interaction generator used in the simulations of the extensive air showers. Based on the generator Sibyll2.3, increased (decreased) fractions of intermediate nuclei (protons) are inferred at all energies (Bellido & Pierre Auger Collaboration 2018). An overall heavier composition is thus implied, in a manner similar to that obtained with the analysis based on EPOS-LHC after a -1σ shift of the X_{\max} scale is applied. The results reported in Appendix C are thus similar to those discussed above when applying the -1σ shift of the X_{\max} scale.

The range of E_{\max}^Z makes the role of the EBL more important than that of the CMB to control the energy losses by the

photodissociation of the nuclei. Consequently, the uncertainties affecting both the far-infrared intensity of the EBL and the partial cross sections of the channels in which α particles are ejected can alter the results. Considering the EBL model of Dominguez et al. (2011) instead of Gilmore et al. (2012) results in an increased far-infrared density of photons, which enhances the intensity of secondary protons from photodissociations en route. Most notably, this enhancement is compensated in the fit to the data through an energy production rate of He (CNO) elements that is increased by $\simeq 25\%$ ($\simeq 45\%$) while that of the protons is decreased by $\simeq 30\%$. Also, the spectral index of protons is increased by +1 for a global deviance similar to that of the benchmark scenario. On the other hand, the cross sections for photodissociation from Puget et al. (1976) and Stecker & Salamon (1999), which neglect α -particle production, impact mainly the balance of the energy production rate of He (CNO) [Si], changing by $\simeq +70\%$ (-45%) [$+20\%$], at the cost of a degraded deviance by 12 units.

Finally, we studied the impact of the redshift evolution of the UHECR luminosity density, considered as flat on large spatial scales in the benchmark scenario. As an alternative to a flat evolution, we tested a scenario where the evolution strictly follows the stellar-mass distribution on large spatial scales (Madau & Dickinson 2014). The only notable difference with the benchmark scenario is a decrease by 20% of the emissivity of all components, which can be understood from the lower average source distance resulting from the decrease of stellar-mass density with redshift at $z > 1$. Another attractive scenario is to assume an evolution proportional to the redshift-dependent star formation rate. Using the corresponding $S(z)$ function derived by Madau & Dickinson (2014), the most notable differences are an increase of the overall energy production rate by a factor 2.5 and a change in the balance of H (He) [CNO] [Si] by $\simeq +40\%$ ($+90\%$) [$+350\%$] [$+25\%$]. In such a scenario, the emissivity would be dominated by a soft proton component and a hard CNO component, with lower mass nuclei partly generated by photodissociation en route from the cosmic-noon epoch at $z > 1$. The quality of the fit is almost unchanged for a source evolution following that of stellar mass or star formation compared to that of the benchmark scenario.

5. Discussion

The results presented in the previous section direct the interpretation of the origin of protons below the ankle energy and of the hard spectra of nuclei above this energy. In this picture, the component of protons is of extragalactic origin well below the ankle energy and exponentially suppressed above it, while heavier nuclei steadily take over to the highest energies through a rigidity-dependent maximum-energy scenario. That the protons do not get suppressed when going down in energy at the same fast rate as the heavier nuclei is modeled by a softer spectral index for this population of low-charge primaries. Interestingly, such a behavior qualitatively fits with scenarios of in-source interactions in which copious fluxes of neutrons, which are produced while accelerated charged particles interact with the bath of photons permeating the sources, escape freely from the electromagnetic fields.

5.1. Comparison with Other Works

Although this scenario has already received considerable attention in recent years (Unger et al. 2015; Globus et al. 2015;

Biehl et al. 2018; Zhang et al. 2018; Fang & Murase 2018; Supanitsky et al. 2018; Boncioli et al. 2019; Muzio et al. 2022), our results provide a robust set of constraints for the spectral indices γ_p and γ_A as well as for the energetics of the sources and for the abundances of elements in their environments. The reason for the robustness of the constraints is twofold. First, the choice to consider the proton spectrum only between 0.63 EeV and 5 EeV allows us to reconstruct the extragalactic component as directly and accurately as possible, without any “interference” from the modeling of the composition of the supposedly upper end of the galactic component. The proton flux in this energy range is indeed generally completed by ad hoc mass components of galactic origin so as to match the all-particle flux and, at most, the first and second moments of X_{\max} or $\ln A$. This leaves some freedom for the modeled proton flux to deviate from the observed one. Second, the deviation from the widely used uniform distribution of sources in a comoving volume, through the addition of a local overdensity, allows us to match the prediction with the data on a statistical basis characterized by $D/\text{ndf} \simeq 237/125$, i.e., a reduced deviance on the order of that found by Aab et al. (2017b) for data strictly above the ankle. The study presented here improves substantially the description of the data, especially the mass-composition sector, compared to previous studies across the ankle reporting goodness-of-fit estimators (Unger et al. 2015; Muzio et al. 2022) while only qualitative trends are generally reported by others. One notable difference, beyond the abundances of elements adjusted to the data in our case, concerns the much softer value of the spectral index γ_p , which can be observed to be generally close to $\gamma_p = 2$ (or even harder) in several studies (Globus et al. 2015; Unger et al. 2015; Biehl et al. 2018). The exploratory finding of $\gamma_p \simeq 2.5$ in the case of protons produced exclusively by in-source interactions might point toward environments largely enriched in intermediate-mass nuclei compared to protons.

5.2. Making up the All-particle Spectrum Below the Ankle Feature

We now comment on the “upper end of the galactic component” not addressed here but needed to complete the picture of the ankle energy range. If protons of extragalactic origin contribute to the sub-ankle component, other elements are needed to make up the all-particle spectrum that, beyond its impressive regularity in the energy region between the second knee near 0.1 EeV and the ankle near 5 EeV, hides beneath a complex intertwining of different astrophysical phenomena. Keeping in mind the reliance of the interpretations of X_{\max} data on the validity of the hadronic interaction models, this intertwining is evidenced by the fraction of elements reported by Bellido & Pierre Auger Collaboration (2018) as a function of energy that can be described broadly as follows. On the one hand, a steep fall-off of the Fe component is observed well below the ankle energy. This is along the lines of the scenario for the bulk of Galactic cosmic rays characterized by a rigidity-dependent maximum acceleration energy, $E_{\max, \text{Gal}}^Z \simeq 3Z \text{ PeV}$, for particles with charge Z to explain the knee structures. On the other hand, all hadronic-interaction models indicate the presence of CNO nuclei between the second-knee and ankle energies. This extra component, which, in the overall scenario explored in this paper, contributes to shape the ankle feature, raises questions. Such intermediate-mass elements could be, for example, fueled by extragalactic sources different from those

Table 3
Best-fit Parameters and Minimum Deviance for Sibyll2.3c

Scenario	γ_p	γ_A	$\log_{10} E_{\max}$ [eV]	$\tilde{\mathcal{L}}_p/\mathcal{L}_0$	$\tilde{\mathcal{L}}_{\text{He}}/\mathcal{L}_0$	$\tilde{\mathcal{L}}_{\text{N}}/\mathcal{L}_0$	$\tilde{\mathcal{L}}_{\text{Si}}/\mathcal{L}_0$	$\tilde{\mathcal{L}}_{\text{Fe}}/\mathcal{L}_0$	D/ndf
$\gamma_p \neq \gamma_A$	3.54 ± 0.25	-0.27 ± 0.08	18.36 ± 0.04	2.97 ± 0.26	1.64 ± 0.11	2.07 ± 0.18	1.12 ± 0.14	0.03 ± 0.05	216.7/125
$\gamma_p = \gamma_A$	γ_A	-0.85 ± 0.15	18.15 ± 0.02	0.55 ± 0.10	1.46 ± 0.10	2.20 ± 0.10	0.78 ± 0.19	0.13 ± 0.10	369.8/126

producing the bulk of UHECRs above the ankle energy (Aloisio et al. 2014). Or, they could correspond to a second Galactic component, as first suggested by Hillas (2005), for example one resulting from explosions of Wolf-Rayet stars (Thoudam et al. 2016).

Other observables could help in providing additional signatures to the general scenario outlined above. One of them relies on measurements of large-scale anisotropies, in particular those discriminated by mass. No significant variation of the all-particle flux across the sky has been revealed so far below the ankle energy. However, the direction in right ascension of the first harmonics shows an intriguing constancy in adjacent energy intervals toward the Galactic center (Aab et al. 2020). This is potentially indicative of a genuine signal (Edge et al. 1978; Deligny 2019). An interesting possibility to explain such a low level of anisotropy could be that one or several mass components are diluted in the extragalactic component of protons, which is expected to be isotropic to a high level due to their interaction lengths comparable to the cosmological horizon. Some estimates of anisotropy show that the most stringent upper limits up to date can then be met for intermediate and heavy nuclei of Galactic origin (Abreu et al. 2012a, 2012b; Giacinti et al. 2012; Pohl & Eichler 2011). Given the increasing contribution of the protons to the flux at the ankle energy, the all-particle anisotropy may even decrease with energy (Deligny 2014), thus providing a mechanism to reduce significantly the amplitude of the vector describing the arrival directions of the whole population of cosmic rays—which is observationally the only one within reach so far. The measurement of mass-discriminated anisotropies in this energy range is challenging; yet the extension to lower energies of directional- $\langle X_{\max} \rangle$ analyses such as presented by Mayotte & Pierre Auger Collaboration (2021) could provide elements to decipher further the origin of the intermediate-mass elements below the ankle energy.

Future observations will thus provide elements helping to corroborate the importance of in-source interactions for the interpretation of UHECR data, or to call for alternative interpretations. One of these alternatives consists in assuming that two extragalactic components, from two distinct types of sources, overlap from below the ankle energy to the highest energies (Aloisio et al. 2014; Mollerach & Roulet 2020; Das et al. 2021; Guido & Pierre Auger Collaboration 2021). If one source type emits only protons, the spectral index of the resulting component was found by Guido & Pierre Auger Collaboration (2021) to be steep ($\simeq 3.30 \pm 0.05$), consistent with the results reported here, while the corresponding cut-off energy is not constrained at high energies. Interestingly, a signature of this scenario would be the presence of a sub-dominant component of protons forming less than 10% of the all-particle flux from $\simeq 10$ EeV up to the highest energies. Such a sub-dominant component could be uncovered, depending on its exact level, with the upgraded instrumentation of the Pierre Auger Observatory in the next years (Castellina & Pierre Auger Collaboration 2019; Aab et al. 2016).

Table 4
Breakdown of Deviance for Sibyll2.3c

Scenario	$D_J (N_J)$	$D_{J_p} (N_{J_p})$	$D_{X_{\max}} (N_{X_{\max}})$	D/ndf
$\gamma_p \neq \gamma_A$	19.7 (15)	001.2 (9)	195.8 (109)	216.7/125
$\gamma_p = \gamma_A$	18.6 (15)	142.0 (9)	209.2 (109)	369.8/126

This work was made possible by with the support of the Institut Pascal at Université Paris-Saclay during the Paris-Saclay Astroparticle Symposium 2021, with the support of the P2IO Laboratory of Excellence (program “Investissements d’avenir” ANR-11-IDEX-0003-01 Paris-Saclay and ANR-10-LABX-0038), the P2I axis of the Graduate School Physics of Université Paris-Saclay, as well as IJCLab, CEA, IPHT, APPEC, the IN2P3 master project UCMN, EuCAPT ANR-11-IDEX-0003-01 Paris-Saclay, and ANR-10-LABX-0038). SM, JB, AC, & OD gratefully acknowledge funding from ANR via the grant Multi-messenger probe of Cosmic Ray Origins (MICRO), ANR-20-CE92-0052. The authors would like to thank colleagues from the Pierre Auger Collaboration for fruitful suggestions, in particular J. M. Gonzalez, S. Mollerach, and E. Roulet for pointing out differences in the normalization of the overdensity parameterization in its cumulated and differential forms, S. Petrer for providing the latest parameterizations of X_{\max} distributions using various hadronic interaction models, and R. Clay and A. Di Matteo for their careful reading and suggestions on the text.

Appendix A

X_{\max} Distributions For the Benchmark Scenario

Figure 3 shows the distributions of the shower-depth maximum, X_{\max} , together with the best-fit models obtained within the benchmark scenario (EPOS-LHC hadronic interaction model).

Appendix B

Deviance For the Benchmark Scenario

Table 2 shows the breakdown of the deviance for the two scenarios: $\gamma_p = \gamma_A$ and $\gamma_p \neq \gamma_A$. The deviance is broken down in three terms as shown in Equation (6).

Appendix C

Best-fit Results For Sibyll2.3c

Tables 3 and 4 shows the best-fit parameters and breakdown of the deviance using Sibyll2.3c as hadronic interaction model instead of EPOS-LHC. As well, Figure 4 shows the energy flux at Earth as a function of energy in the case of Sibyll2.3c. Although the latest version of Sibyll is Sibyll2.3d (Riehn et al. 2020), Sibyll2.3c is used here as a matter of consistency to match the analysis of Bellido & Pierre Auger Collaboration (2018), which provides the fractions used to derive the proton flux. For completeness, the analysis has also been run using

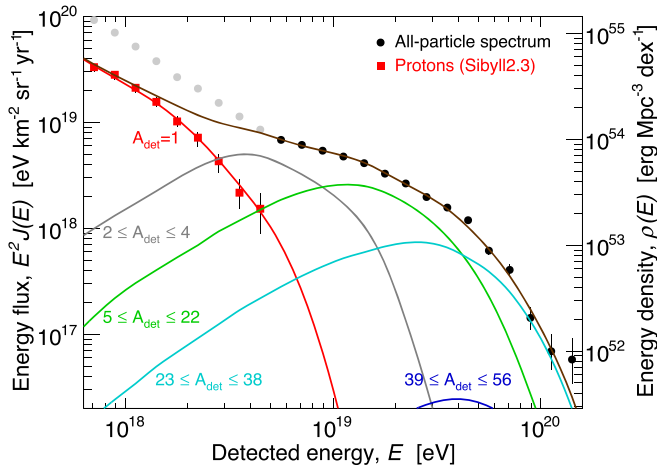


Figure 4. Energy flux at Earth as a function of energy, as modeled by the best-fit parameters for a variation around the benchmark scenario using the Sibyll2.3c hadronic interaction model. The all-particle spectrum and proton component are shown as black circles and red squares, respectively. Lighter points are not included in the fit. The best-fit components obtained for the five detected mass groups are displayed with solid colored lines, as labeled in the figure.

Sibyll2.3d. It results in similar best-fit parameters, with, however, a composition deviance increased by ~ 20 units.

ORCID iDs

Quentin Luce <https://orcid.org/0000-0003-3745-6709>
 Sullivan Marafico <https://orcid.org/0000-0003-4604-4677>
 Jonathan Biteau <https://orcid.org/0000-0002-4202-8939>
 Antonio Condorelli <https://orcid.org/0000-0001-5681-0086>
 Olivier Deligny <https://orcid.org/0000-0001-6863-6572>

References

Aab, A., Abreu, P., Aglietta, M., et al. 2014a, *PhRvD*, **90**, 122006
 Aab, A., Abreu, P., Aglietta, M., et al. 2014b, *PhRvD*, **90**, 122005
 Aab, A., Abreu, P., Aglietta, M., et al. 2015, *NIMPA*, **798**, 172
 Aab, A., Abreu, P., Aglietta, M., et al. 2016, arXiv:1604.03637
 Aab, A., Abreu, P., Aglietta, M., et al. 2017a, *Sci*, **357**, 1266
 Aab, A., Abreu, P., Aglietta, M., et al. 2017b, *JCAP*, **04**, 038
 Aab, A., Abreu, P., Aglietta, M., et al. 2018a, *ApJ*, **868**, 4
 Aab, A., Abreu, P., Aglietta, M., et al. 2018b, *ApJL*, **853**, L29
 Aab, A., Abreu, P., Aglietta, M., et al. 2020, *ApJ*, **891**, 142
 Abraham, J., Abreu, P., Aglietta, M., et al. 2010, *PhRvL*, **104**, 091101
 Abreu, P., Aglietta, M., Ahlers, M., et al. 2012a, *ApJL*, **762**, L13
 Abreu, P., Aglietta, M., Ahlers, M., et al. 2012b, *ApJS*, **203**, 34
 Abreu, P., Aglietta, M., Albury, J.M., et al. 2021, *EPJC*, **81**, 966
 Ackermann, M., Ajello, M., Baldini, L., et al. 2018, *ApJS*, **237**, 32
 Allard, D., Busca, N. G., Decerprit, G., Olinto, A. V., & Parizot, E. 2008, *JCAP*, **10**, 033
 Aloisio, R., Berezhinsky, V., & Blasi, P. 2014, *JCAP*, **10**, 020
 Aloisio, R., Boncioli, D., di Matteo, A., et al. 2016, arXiv:1602.01239

Aloisio, R., Boncioli, D., di Matteo, A., et al. 2015, arXiv:1505.01347
 Aloisio, R., Boncioli, D., Grillo, A. F., Petrer, S., & Salamida, F. 2012, *JCAP*, **10**, 007
 Alves Batista, R., & Saveliev, A. 2021, *Univ*, **7**, 223
 Apel, W. D., Arteaga-Velázquez, J.C., Bekk, K., et al. 2012, *Aph*, **36**, 183
 Bellido, J. & Pierre Auger Collaboration 2018, *PoS, ICRC2017*, 506
 Biehl, D., Boncioli, D., Fedynitch, A., & Winter, W. 2018, *A&A*, **611**, A101
 Biteau, J., & Meyer, M. 2022, *Galax*, **10**, 39
 Biteau, J. & Pierre Auger Collaboration 2021, *PoS, ICRC2021*, 307
 Boncioli, D., Biehl, D., & Winter, W. 2019, *ApJ*, **872**, 110
 Castellina, A. & Pierre Auger Collaboration 2019, *EPJWC*, **210**, 06002
 Condon, J. J., Matthews, A. M., & Broderick, J. J. 2019, *ApJ*, **872**, 148
 Das, S., Razaque, S., & Gupta, N. 2021, *EPJC*, **81**, 59
 Deligny, O. 2014, *CRPhy*, **15**, 367
 Deligny, O. 2019, *Aph*, **104**, 13
 Dominguez, A., Primack, J.R., Rosario, D.J., et al. 2011, *MNRAS*, **410**, 2556
 Edge, D. M., Pollock, A. M. T., Reid, R. J. O., Watson, A. A., & Wilson, J. G. 1978, *J. Phys. G*, **4**, 133
 Fang, K., & Murase, K. 2018, *NatPh*, **14**, 396
 Fujita, Y., Ohira, Y., Tanaka, S. J., & Takahara, F. 2009, *ApJL*, **707**, L179
 Giacinti, G., Kachelriess, M., Semikoz, D. V., & Sigl, G. 2012, *JCAP*, **07**, 031
 Gilmore, R. C., Somerville, R. S., Primack, J. R., & Dominguez, A. 2012, *MNRAS*, **422**, 3189
 Globus, N., Allard, D., & Parizot, E. 2015, *PhRvD*, **92**, 021302
 Guido, E. & Pierre Auger Collaboration 2021, *PoS, ICRC2021*, 311
 Hillas, A. M. 2005, *J. Phys. G*, **31**, R95
 Jedamzik, K., & Saveliev, A. 2019, *PhRvL*, **123**, 021301
 Koning, A. J., Hilaire, S., & Duijvestijn, M. C. 2005, in INTERNATIONAL CONFERENCE ON NUCLEAR DATA FOR SCIENCE AND TECHNOLOGY. AIP Conf. Proc. 769 (San Francisco, CA: ASP), 1154
 Koning, A. J., & Rochman, D. 2012, *NDS*, **113**, 2841
 Madau, P., & Dickinson, M. 2014, *ARA&A*, **52**, 415
 Mayotte, E. & Pierre Auger Collaboration 2021, *PoS, ICRC2021*, 321
 McCall, M. L. 2014, *MNRAS*, **440**, 405
 Mollerach, S., & Roulet, E. 2013, *JCAP*, **10**, 013
 Mollerach, S., & Roulet, E. 2020, *PhRvD*, **101**, 103024
 Muzio, M. S., Farrar, G. R., & Unger, M. 2022, *PhRvD*, **105**, 023022
 Neronov, A., & Vovk, I. 2010, *Sci*, **328**, 73
 O'Sullivan, S. P., Brügggen, M., Vazza, F., et al. 2020, *MNRAS*, **495**, 2607
 Pierog, T., Karpenko, I., Katzy, J. M., Yatsenko, E., & Werner, K. 2015, *PhRvC*, **92**, 034906
 Pohl, M., & Eichler, D. 2011, *ApJ*, **742**, 114
 Pshirkov, M. S., Tinyakov, P. G., & Urban, F. R. 2016, *PhRvL*, **116**, 191302
 Pueschel, E., & Biteau, J. 2021, arXiv:2112.05952
 Puget, J. L., Stecker, F. W., & Bredekamp, J. H. 1976, *ApJ*, **205**, 638
 Riehn, F., Dembinski, H. P., Engel, R., et al. 2017, *PoS, ICRC2017*, 301
 Riehn, F., Engel, R., Fedynitch, A., Gaisser, T. K., & Stanev, T. 2020, *PhRvD*, **102**, 063002
 Sironi, L., Keshet, U., & Lemoine, M. 2015, *SSRv*, **191**, 519
 Stecker, F. W., & Salamon, M. H. 1999, *ApJ*, **512**, 521
 Supanitsky, A. D., Cobos, A., & Etchegoyen, A. 2018, *PhRvD*, **98**, 103016
 Tavecchio, F., Ghisellini, G., Foschini, L., et al. 2010, *MNRAS*, **406**, L70
 Taylor, A. M., Ahlers, M., & Hooper, D. 2015, *PhRvD*, **92**, 063011
 Thoudam, S., Rachen, J. P., van Vliet, A., et al. 2016, *A&A*, **595**, A33
 Unger, M., Farrar, G. R., & Anchordoqui, L. A. 2015, *PhRvD*, **92**, 123001
 Vazza, F., Brügggen, M., Gheller, C., et al. 2017, *CQG*, **34**, 234001
 Watson, A. A. 2022, *JHEAp*, **33**, 130
 Wittkowski, D. 2018, *PoS, ICRC2017*, 563
 Zhang, B. T., Murase, K., Kimura, S. S., Horiuchi, S., & Mészáros, P. 2018, *PhRvD*, **97**, 083010